752 *Biochemistry* **2010,** *49,* 752–760
DOI: 10.1021/bi901599u

BIOCHEMISTRY
including biophysical chemistry & molecular biology
Article

Structural and Functional Studies of *Aspergillus clavatus* N^5-Carboxyaminoimidazole Ribonucleotide Synthetase[†,‡]

James B. Thoden,[§] Hazel M. Holden,*,[§] Hanumantharao Paritala,[‖] and Steven M. Firestine*,[‖]

[§]*Department of Biochemistry, University of Wisconsin, Madison, Wisconsin 53706 and* [‖]*Department of Pharmaceutical Sciences, Eugene Applebaum College of Pharmacy and Health Sciences, Wayne State University, Detroit, Michigan 48201*

Received September 11, 2009; Revised Manuscript Received November 20, 2009

ABSTRACT: N^5-Carboxyaminoimidazole ribonucleotide synthetase (N^5-CAIR synthetase), a key enzyme in microbial de novo purine biosynthesis, catalyzes the conversion of aminoimidazole ribonucleotide (AIR) to N^5-CAIR. To date, this enzyme has been observed only in microorganisms, and thus, it represents an ideal target for antimicrobial drug development. Here we report the cloning, crystallization, and three-dimensional structural analysis of *Aspergillus clavatus* N^5-CAIR synthetase solved in the presence of either Mg_2ATP or MgADP and AIR. These structures, determined to 2.1 and 2.0 Å, respectively, revealed that AIR binds in a pocket analogous to that observed for other ATP-grasp enzymes involved in purine metabolism. On the basis of these models, a site-directed mutagenesis study was subsequently conducted that focused on five amino acid residues located in the active site region of the enzyme. These investigations demonstrated that Asp 153 and Lys 353 play critical roles in catalysis without affecting substrate binding. All other mutations affected substrate binding and, in some instances, catalysis as well. Taken together, the structural and kinetic data presented here suggest a catalytic mechanism whereby Mg_2ATP and bicarbonate first react to form the unstable intermediate carboxyphosphate. This intermediate subsequently decarboxylates to CO_2 and inorganic phosphate, and the amino group of AIR, through general base assistance by Asp 153, attacks CO_2 to form N^5-CAIR.

Arguably, one of the most important developments in the history of modern medicine has been the discovery of antibiotics. The golden age of antibacterial drug discovery began during the 1940s, and by the beginning of the 1970s, most of the major classes of antibiotics currently in clinical use had been discovered (*1*, *2*). The rate of antimicrobial drug discovery has since slowed as evidenced by the fact that only two new classes of antibiotics, the lipopeptides and the oxazolidinones, have been brought to the market within the past 40 years (*3*, *4*). Unfortunately, as the pharmaceutical industry's interest in antibiotic drug discovery has waned, resistance to existing antibiotics has grown. Recent studies have shown that approximately 50% of all *Staphylococcus aureus* infections are methicillin resistant, and strikingly, *S. aureus* resistance to most other existing antibiotics has been detected in clinical settings (*1*, *5*, *6*). These results foreshadow the day in which bacteria become resistant to all known antibiotics.

The increasing prevalence of antibiotic resistant infections has led to a recent, renewed interest in antibiotic drug development. For example, studies have examined enzymes such as pantothenate kinase (*7*), tRNA synthetase (*8*), and DNA ligase (*9*), or biosynthetic pathways such as those for the production of isoprenoids (*10*) and aromatic amino acid synthesis (*11*), as potential antibacterial drug targets. One unexplored pathway for antimicrobial drug design is de novo purine biosynthesis, which is markedly different in microorganisms and humans (*12*−*16*). As revealed in studies conducted in the 1980s, bacteria, yeast, and fungi synthesize the purine intermediate, inosine monophosphate (IMP), via 11 enzymatic steps, whereas in humans, only 10 steps are required. The additional step is catalyzed by the enzyme N^5-carboxyaminoimidazole ribonucleotide (N^5-CAIR) synthetase, which converts 5-aminoimidazole ribonucleotide (AIR)[1] to N^5-carboxyaminoimidazole ribonucleotide (N^5-CAIR) as indicated in Scheme 1 (*12*, *13*, *16*). This activity is not required for the synthesis of IMP in humans, and since humans have no homologues for this enzyme, N^5-CAIR synthetase represents an attractive target for drug development. Indeed, we have discovered a series of small, druglike inhibitors of this enzyme and have shown that these agents inhibit bacterial growth on purine deficient media (*17*).

To further our drug discovery efforts and to enhance our understanding of N^5-CAIR synthetase, we embarked on a series of structural and enzymological investigations. Recently, our laboratories reported the molecular structures of the Mg/ATP and Mg/ADP·P_i complexes of N^5-CAIR synthetase from *Escherichia coli* (*18*). These two models provided us with a detailed view of the protein before and after ATP hydrolysis, and we were able to use this information to suggest a possible catalytic

---

[†] This research was supported in part by National Institutes of Health Grants DK47814 to H.M.H. and GM087467 to S.M.F.

[‡] X-ray coordinates have been deposited in the Research Collaboratory for Structural Bioinformatics, Rutgers University (Protein Data Bank entries 3K5H and 3K5I).

*To whom correspondence should be addressed. E-mail: sfirestine@wayne.edu or hazel_holden@biochem.wisc.edu. Fax: (313) 577-2033. Phone: (313) 577-0455.

[1] Abbreviations: AIR, 5-aminoimidazole ribonucleotide; AMPPNP, adenosine 5′-(β,γ-imido)triphosphate; CAIR, 4-carboxy-5-aminoimidazole ribonucleotide; CHES, *N*-cyclohexyl-2-aminoethanesulfonic acid; MWC, molecular weight cutoff; Tris, tris(hydroxymethyl)-aminomethane.

Scheme 1

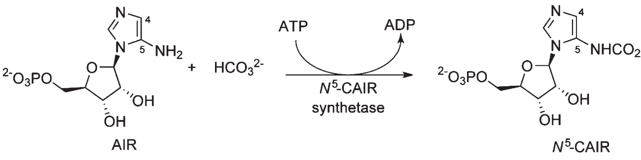

mechanism for the enzyme. Unfortunately, numerous efforts aimed at obtaining the structure of the enzyme in the presence of AIR failed. Due to the mechanistic, structural, and medicinal importance of this information, we initiated a study of N^5-CAIR synthetase from *Aspergillus clavatus,* a common soil fungus. As observed in other eukaryotic microorganisms, the *A. clavatus* N^5-CAIR synthetase exists as a bifunctional protein with the next enzyme in the pathway, N^5-CAIR mutase (*16*). For this investigation, we cloned only the N^5-CAIR synthetase domain, overexpressed and purified the protein, and determined its structure in the presence of either Mg_2ATP or MgADP and AIR. In addition, we changed five key residues in the AIR binding pocket (Glu 73, Tyr 152, Asp 153, Arg 155, and Lys 353) via site-directed mutagenesis to probe their function within the active site of the enzyme. Taken together, these studies provide new, detailed information on those residues critical for substrate binding and for catalysis in the N^5-CAIR synthetases.

MATERIALS AND METHODS

Cloning, Expression, and Purification. Genomic DNA from *A. clavatus* (ATCC 1007) was isolated by standard procedures. The fragment of the ADE2 gene encoding N^5-CAIR synthetase (residues 1−383) was polymerase chain reaction-amplified using primers that introduced 5′ NdeI and 3′ NotI sites. The purified polymerase chain reaction (PCR) product was A-tailed and ligated into a pGEM-T (Promega) vector for screening and sequencing. Subsequently, two introns present in the gene encoding N^5-CAIR synthetase were excised by mutagenesis. PurK-pGEM-T vector constructs of the correct sequence were then appropriately digested and ligated into a pET28b(+) (Novagen) plasmid for protein expression with an N-terminal His tag of the following sequence (MGSSHHHHHHSSENLYFQGH).

The N^5-CAIR synthetase-pET28 plasmid was used to transform HMS174(DE3) *E. coli* cells (Novagen). The cultures in Luria-Bertani media were grown at 37 °C with shaking until an optical density of ~0.8 was measured at 600 nM. The cultures were then cooled to 16 °C; isopropyl β-D-1-thiogalactopyranoside was added to a final concentration of 1.0 mM, and induction was allowed to proceed for 18 h. N^5-CAIR synthetase was purified by standard methods with nickel nitrilotriacetic acid resin. Purified N^5-CAIR synthetase was dialyzed against 10 mM Tris-HCl and 200 mM NaCl (pH 8). Following dialysis, the sample was concentrated to ~15 mg/mL and frozen in liquid nitrogen.

To investigate the roles of Glu 73, Tyr 152, Asp 153, Arg 155, and Lys 353 in the catalytic mechanism of N^5-CAIR synthetase, the following point mutations were constructed via the Stratagene QuikChange method: E73A, Y152A, D153A, R155A, and K353A. All modified genes were sequenced to verify that no other changes had been inadvertently introduced. Mutant proteins were expressed and purified in the manner described for the wild-type enzyme.

Structural Analysis of N^5-CAIR Synthetase. Crystallization conditions were initially surveyed by the hanging drop method of vapor diffusion with a sparse matrix screen developed in the laboratory, using the protein incubated with 10 mM ATP and 40 mM $MgCl_2$. X-ray diffraction quality crystals were grown via the hanging drop method against 15−19% monomethylether poly(ethylene glycol) 5000 and 200 mM NaCl buffered with 100 mM CHES (pH 9.0). The crystals belonged to space group $P2_1$ with two dimers per asymmetric unit and the following unit cell dimensions: $a = 75.9$ Å, $b = 134.5$ Å, $c = 99.6$ Å, and $\beta = 107.0°$.

Table 1: X-ray Data Collection Statistics

	enzyme complexed with Mg_2ATP	enzyme complexed with MgADP and AIR
space group	$P2_1$	$P2_1$
resolution limits (Å)	30.0−2.1 (2.2−2.1)[b]	30.0−2.0 (2.1−2.0)[b]
no. of independent reflections	104348 (12740)[b]	118616 (15717)[b]
completeness (%)	93.6 (86.5)[b]	91.9 (86.4)[b]
redundancy	4.0 (1.8)[b]	2.9 (1.5)[b]
avg I/avg $\sigma(I)$	9.6 (2.2)[b]	7.3 (2.0)[b]
R_{sym} (%)[a]	8.7 (30.9)[b]	8.9 (28.6)[b]

[a] $R_{sym} = (\sum|\sum I - \bar{I}|/\sum I)\times 100$. [b] Statistics for the highest-resolution bin.

Native X-ray data were measured at 100 K using a Bruker AXS Platinum 135 CCD detector controlled with the Proteum software suite (Bruker AXS Inc.). The X-ray source was Cu Kα radiation from a Rigaku RU200 X-ray generator equipped with Montel optics and operated at 50 kV and 90 mA. These X-ray data were processed with SAINT version 7.06A (Bruker AXS Inc.) and internally scaled with SADABS version 2005/1 (Bruker AXS Inc.). Prior to X-ray data collection at 100 K, the crystals were stabilized by being transferred into a 25% monomethylether poly(ethylene glycol) 5000 solution containing 400 mM NaCl, 10 mM ATP, 40 mM $MgCl_2$, and 15% ethylene glycol.

In an attempt to prepare a ternary complex of N^5-CAIR synthetase with MgAMPPNP and AIR, crystals of the apoenzyme were grown under the same conditions described above and subsequently soaked in 10 mM AMPPNP, 40 mM $MgCl_2$, and 10 mM AIR for 18 h. Unfortunately, the ATP analogue hydrolyzed to ADP. We tried substituting AMPPCP for AMPPNP, but the crystals did not diffract well. A low-resolution structure demonstrated that the AMPPCP bound in a nonproductive manner relative to that observed for ATP in the enzyme·Mg_2ATP complex. Hence, the ternary complex reported here is that of the enzyme with MgADP and AIR. Relevant X-ray data collection statistics for both protein complexes are listed in Table 1.

The structure of N^5-CAIR synthetase in complex with Mg_2ATP was solved by molecular replacement with the program Phaser (*19*) using as a search model the structure of the apo form of *Candida albicans* N^5-CAIR synthetase determined in this laboratory (unpublished results). The initial electron density map was subsequently improved by 4-fold averaging with the software package DM (*20*). An initial model was built using COOT (*21*). Least-squares refinement with TNT (*22*) and manual adjustment with COOT reduced the *R*-factor to 19.8% for all measured X-ray data from 30 to 2.1 Å resolution. The coordinates for this structure served as the starting model for refinement of the enzyme·MgADP·AIR complex. Least-squares refinement of the enzyme·MgADP·AIR complex converged to 20.6% for all measured X-ray data from 30 to 2.0 Å resolution. Relevant refinement statistics are listed in Table 2.

Kinetic Analyses of Wild-Type and Mutant Enzymes. The steady-state kinetic parameters for the wild-type and mutant

Table 2: Least-Squares Refinement Statistics

	enzyme complexed with Mg_2ATP	enzyme complexed with MgADP and AIR
resolution limits (Å)	30.0−2.1	30.0−2.0
R-factor[a] (overall) (%)/no. of reflections	19.8 (104194)	20.6 (118549)
R-factor (working) (%)/no. of reflections	19.6 (93863)	20.3 (106822)
R-factor (free) (%)/no. of reflections	26.1 (10331)	26.9 (11667)
no. of protein atoms	11869[b]	11802[c]
no. of heteroatoms	981[d]	1345[e]
average *B* values		
protein atoms ($Å^2$)	32.8	32.7
ligands ($Å^2$)	30.8	30.0
solvent ($Å^2$)	35.7	
weighted root-mean-square deviations from ideality		
bond lengths (Å)	0.012	0.014
bond angles (deg)	2.60	2.83
trigonal planes (Å)	0.007	0.008
general planes (Å)	0.012	0.012
torsional angles[f] (deg)	18.3	18.8
Ramachandran Statistics [core, allowed, generously allowed (%)]	89.5, 10.3, 0.2	89.3, 10.5, 0.2

[a] *R*-factor = $(\sum|F_o - F_c|/\sum|F_o|) \times 100$, where F_o is the observed structure factor amplitude and F_c is the calculated structure factor amplitude. [b] These include multiple conformations for Asn 37, Cys 67, Gln 96, and Ser 339 in chain A, Gln 62, Glu 171, Glu 236, Asp 246, and Glu 259 in chain B, Arg 61 and Asn 231 in chain C, and Val 9 in chain D. [c] These include multiple conformations for Asp 47, Lys 65, Gln 327, Ser 339, and His 365 in chain A, Gln 62, Asp 78, Glu 120, Lys 233, Asp 246, and Glu 259 in chain B, Gln 29, Asp 47, Lys 65, Gln 96, Arg 112, and Glu 236 in chain C, and Ser 4 in chain D. [d] Heteroatoms include 4 ATP, 8 Mg^{2+}, and 849 waters. [e] Heteroatoms include 4 ADP, 4 Mg^{2+}, 4 AIR, 1 Na^+, 2 CHES, and 1130 waters. [f] The torsional angles were not restrained during the refinement.

enzymes were determined using the ATP-coupled assay system as previously described (*17*). In a 1 mL cuvette, buffer [50 mM HEPES (pH 7.5), 20 mM KCl, and 6.0 mM $MgCl_2$], 0.2 mM NADH, 2.0 mM phosphoenolpyruvate, 1.0 mM $NaHCO_3$, 4 units of pyruvate kinase, and 17 units of lactate dehydrogenase were added. After the cuvette was equilibrated to 37 °C, N^5-CAIR synthetase was added (the amount varied depending upon the mutant protein) followed by 1.1 mM ATP. Background levels of ATP hydrolysis were measured, and the reaction was initiated by the addition of AIR (concentration varied from 5 to 500 μM). NADH oxidation was monitored at 340 nm, and the concentration of AIR consumed was calculated using the extinction coefficient for NADH (6200 M^{-1} cm^{-1}). The background ATPase activity was very low (< 0.5%) and thus was not subtracted from the initial velocity. The initial velocity of each reaction was determined during the first 2 min, and a plot of initial velocity versus AIR concentration was generated. Kinetic parameters were determined by fitting multiple data sets to the Michaelis−Menten equation using KaleidaGraph. Reported errors are those generated from the curve fit.

Equilibrium Dialysis of Wild-Type and Mutant Enzymes. The dissociation constant for AIR was determined by equilibrium dialysis. To conduct these experiments, 200 μL of enzyme (final concentration of 10−12 μM based upon a dimer molecular weight) in 50 mM HEPES (pH 7.5), 20 mM KCl, and 6.0 mM $MgCl_2$ buffer was added to six dialysis tubes (MWC of 8000). Simultaneously, six glass vials containing 1.5 mL of one of six AIR concentrations (from 1 to 300 μM in the same buffer as the enzyme) were prepared, and the absorbance of each solution was determined at 250 nm. The concentration of AIR was determined using the published extinction coefficient of 3270 M^{-1} cm^{-1} (*12*). One dialysis tube was added to each vial, and the vials were placed into a shaker incubator and gently shaken for 16 h at room temperature. After dialysis, the concentration of free AIR was determined by the absorbance at 250 nm using the extinction coefficient listed above. The concentration of bound AIR was determined by subtracting the amount of free AIR from the total amount of AIR added at the beginning of the experiment. Control experiments conducted in the absence of enzyme revealed no change in AIR concentration, indicating that the substrate was stable over the course of the experiment. Control experiments of the enzymes in the absence of substrate revealed that they lost 10−20% of their activity during shaking at room temperature over the 16 h period. The dissociation constants and enzyme concentrations were determined by fitting the data from a plot of the total amount of AIR versus the amount of bound AIR to eq 1

$$\mathrm{AIR_{bound}} = \left[E_T + \mathrm{AIR_T} + K_d - \sqrt{(E_T + \mathrm{AIR_T} + K_d)^2 - 4E_T\mathrm{AIR_T}}\right]/2E_T \quad (1)$$

where E_T is the total enzyme concentration, $\mathrm{AIR_T}$ is the total AIR concentration, $\mathrm{AIR_{bound}}$ is the amount of AIR bound to the enzyme, and K_d is the dissociation constant. Reported errors are those generated from the curve fit.

RESULTS AND DISCUSSION

Structure of N^5-CAIR Synthetase Complexed with Mg_2ATP. N^5-CAIR synthetase from the bifunctional ADE2-encoded protein was cloned, expressed, purified, and crystallized as described in Materials and Methods. It is a dimer with overall dimensions of ~90 Å × 80 Å × 60 Å and a total buried surface area of 3600 $Å^2$. Each subunit of the dimer folds into three domains that are referred to as A, B, and C and that extend from Met 1 to Ala 119, from Glu 120 to Trp 183, and from Ala 184 to Arg 382, respectively (Figure 1). The A domain is characterized by a five-stranded parallel β-sheet flanked on each side by two α-helices. Two additional α-helices, oriented at approximately 90° with respect to one another and connected by Asn 103, provide a bridge from the A domain to the B domain. This helix−residue−helix motif is a structural hallmark for enzymes belonging to the ATP-grasp superfamily. The B domain contains a four-stranded antiparallel β-sheet, which is covered on one side by two α-helices. The C domain is the most complicated of the three motifs with a total of nine β-strands that form a decidedly twisted antiparallel β-sheet. Whereas the A and C domains contribute to the subunit−subunit interface, the B domains splay away from the main body of the molecule, and the temperature factors for the residues forming this domain are typically higher than those found in the A and C domains. There are three residues that adopt cis-peptide bonds, Pro 93 in the A domain, Pro 142 in the B domain, and Pro 222 in the C domain. None of these is located near the active site.

The crystals used in this investigation contained two dimers in the asymmetric unit, and the α-carbons for the four subunits superimpose with root-mean-square deviations (rmsds) as low as

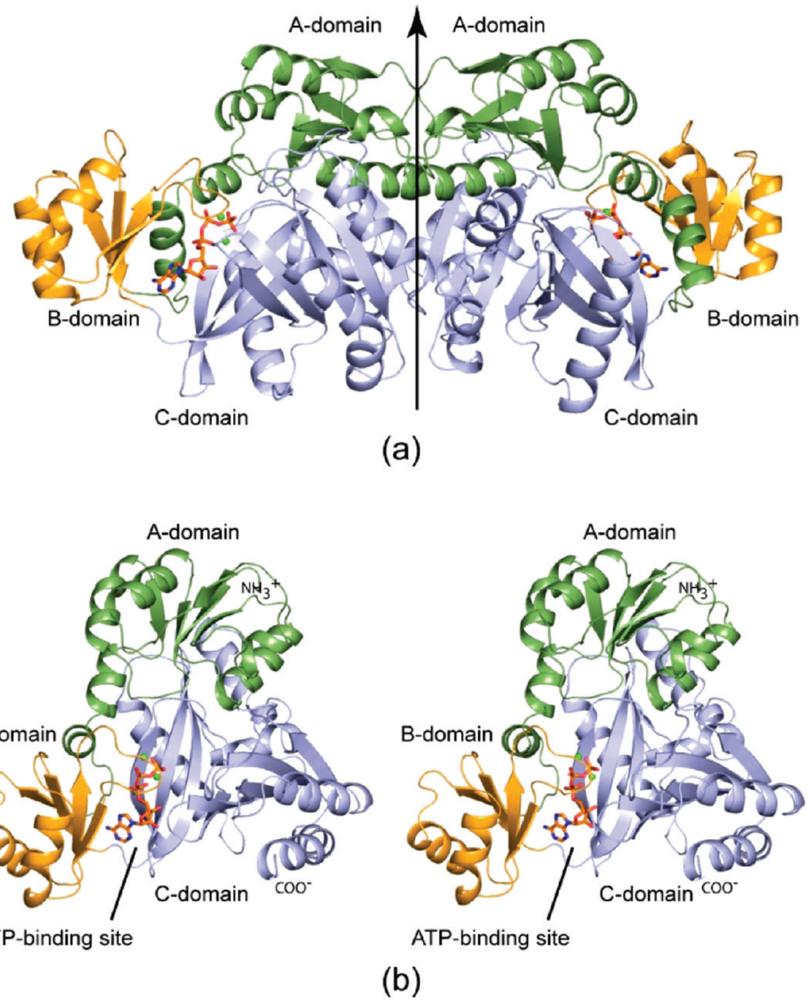

FIGURE 1: Overall molecular structure of N^5-CAIR synthetase from *A. clavatus*. (a) Ribbon representation of the N^5-CAIR synthetase dimer. The molecular dyad relating one subunit to the other is indicated by the black arrow. Each subunit folds into three motifs referred to as the A, B, and C domains. The ATP ligands, depicted in stick representations, are wedged between the B and C domains. (b) Stereoview of subunit 2 of the dimer. The magnesium ions are shown as green spheres, whereas the ATP ligands are displayed as sticks. Ordered water molecules are represented as red spheres. All figures were prepared with PyMOL (*24*).

0.24 Å or as high as 0.98 Å. These differences result from variations in the orientations of the B domains relative to the A and C domains. Overall, the quality of the electron density was best for subunit 2 in the X-ray coordinate file, and thus, the following discussion refers only to it. Electron density corresponding to the bound ATP is displayed in Figure 2a. As can be seen, two magnesium ions accompany the ATP in the active site. One of these is wedged between an α- and a γ-phosphoryl oxygen, whereas the other is situated between a β- and a γ-phosphoryl oxygen. The ribose of the nucleotide adopts the $C_{3'}$-*endo* pucker.

A close-up view of the active site is presented in Figure 2b. With the exception of Lys 104, all of the residues responsible for binding the nucleotide are contributed by the B and C domains. Both magnesium ions are octahedrally coordinated with metal–ligand bond distances ranging from 1.8 to 2.4 Å. Magnesium ion "A" is surrounded by Glu 254, Glu 267, two phosphoryl oxygens, and a water molecule. Glu 254 functions as a bidentate ligand. Magnesium ion "B" is ligated by Glu 267, two phosphoryl oxygens, and two waters. Glu 267 not only functions as a bidentate ligand but also serves to bridge the two cations together. The metal binding geometry observed for the *A. clavatus* N^5-CAIR synthetase is nearly identical to that previously reported for the enzyme from *E. coli* (*18*). Two lysine residues, namely, Lys 104 and Lys 146, provide additional positive charges to further neutralize the negatively charged phosphoryl groups of ATP. The adenine ring is anchored into the active site by hydrogen bonding with two side chains, Lys 146 and Glu 181, and with the carbonyl oxygen of Lys 182 and the backbone amide nitrogen of Ala 184. There is an additional hydrogen bond between the adenine ring and a water molecule. Both the 2- and 3-hydroxyls of the ribose lie within hydrogen bonding distance to the carboxylate of Glu 189. The indole ring of Trp 183 forms a T-shaped stacking interaction with the adenine ring.

Structure of N^5-CAIR Synthetase Complexed with MgADP and AIR. As in the case of the structure analysis of N^5-CAIR synthetase complexed with Mg_2ATP, the crystals used to trap MgADP and AIR contained two dimers in the asymmetric unit. The four individual subunits correspond with root-mean-square deviations between 0.25 and 1.5 Å. Again, these differences arise from the flexibility of the B domains relative to the main body of the enzyme. In this X-ray analysis, subunit 3 displayed the best overall electron density, and thus, the following discussion refers only to it.

As shown in Figure 3a, the electron densities for ADP and AIR are very well ordered. Only one magnesium ion is observed lying between an α- and a β-phosphoryl oxygen of ADP. The AIR ribose adopts the $C_{3'}$-*endo* pucker. A distance of ~8 Å

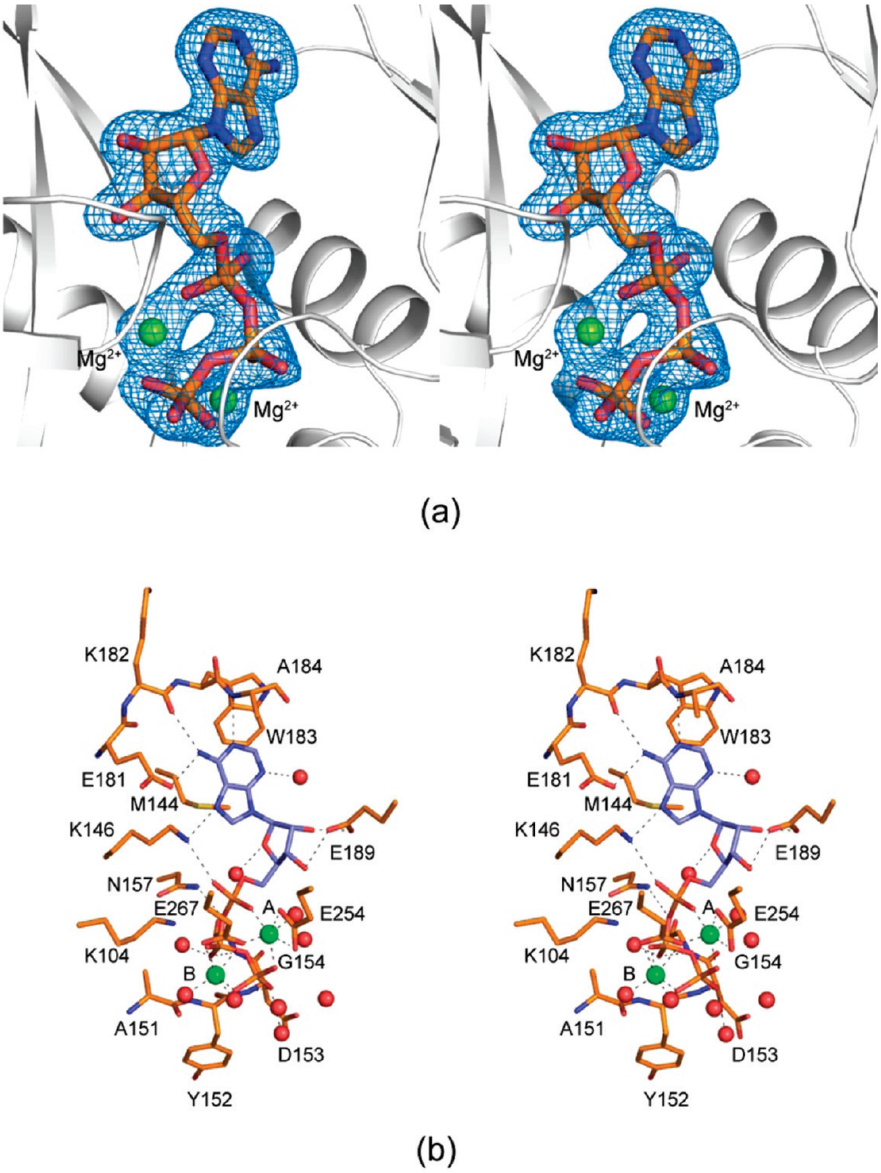

FIGURE 2: Structure of N^5-CAIR synthetase in complex with Mg$_2$ATP. (a) Stereoview of the electron density corresponding to the two magnesium ions and the nucleotide. The map was contoured at 3.5σ and calculated with coefficients of the form $F_o - F_c$, where F_o is the native structure factor amplitude and F_c the calculated structure factor amplitude. (b) Close-up view of the Mg$_2$ATP binding pocket. Those residues located within ~3.6 Å of the Mg$_2$ATP are shown with gold bonds. The nucleotide and the magnesium ions are highlighted as blue filled bonds and green spheres, respectively. Possible hydrogen bonding interactions are indicated by the dashed lines. The coordination geometries about the magnesiums are also shown as dashed lines.

separates the two ligands. The position of the B domain in the MgADP·AIR complex moves slightly towards a more closed conformation than that observed for the Mg$_2$ATP complex. Overall, however, the polypeptide chains for the two enzyme complexes presented here are very similar and correspond with a root-mean-square deviation of 1.1 Å.

A close-up view of the active site is presented in Figure 3b. As might be expected, the hydrogen bonding patterns surrounding the adenine ring and the ribose of the ADP ligand are similar to those observed for ATP. The sole magnesium ion is octahedrally coordinated by two phosphoryl oxygens, two water molecules, and the side chains of Glu 254 and Glu 267. Glu 254 no longer functions as a bidentate ligand. Metal−ligand bond distances range from 1.9 to 2.4 Å.

The 5-aminoimidazole moiety of AIR is firmly anchored into the active site via hydrogen bonding interactions with three water molecules and the carboxylate group of Asp 153. One of these waters serves as a bridge between the 5-aminoimidazole moiety, the ribose ring oxygen, and the bridging phosphoryl oxygen. Glu 73 forms a hydrogen bond to the 2- and 3-hydroxyls of the ribose, whereas the positively charged side chains of Arg 155, Lys 345, and Arg 352 participate in electrostatic interactions with the phosphoryl group. Tyr 152 also provides a hydrogen bond to a phosphoryl oxygen of the AIR ligand.

Analysis of Site-Directed Mutant Proteins of N^5-CAIR Synthetase. The availability of the MgADP·AIR structure provided us with the necessary information to begin to assess the function of amino acids located in the active site of the enzyme. The investigations reported here focused on the AIR binding site and in particular targeted five residues (Glu 73, Tyr 152, Asp 153, Arg 155, and Lys 353) for site-directed mutagenesis and analysis. Note that Lys 353 does not directly hydrogen bond to AIR but rather lies within 2.6 Å of the carboxylate of Asp 153 (Figure 3b).

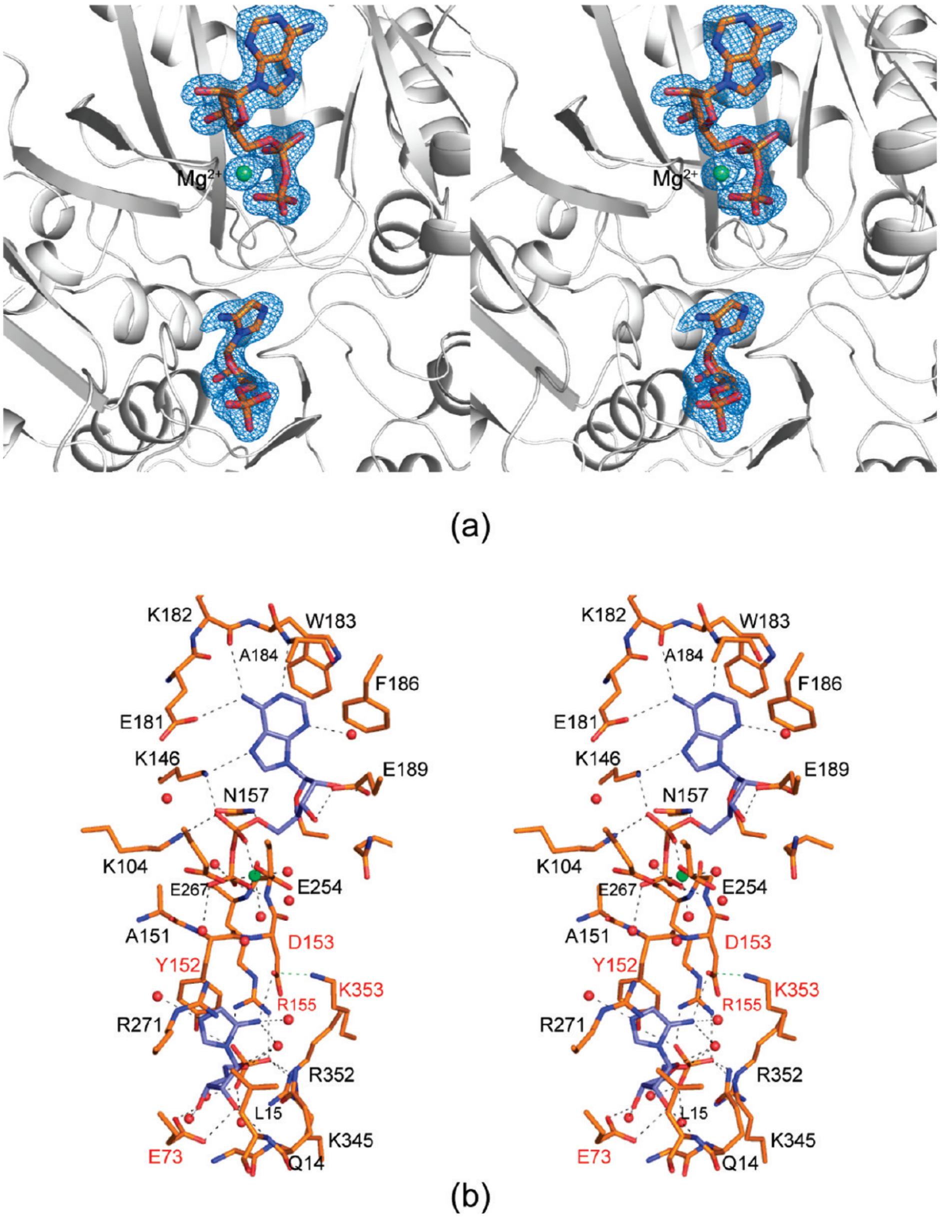

Figure 3: Structure of N^5-CAIR synthetase in complex with MgADP and AIR. (a) Electron density corresponding to the two ligands. The map was calculated and contoured as described in the legend of Figure 2a. (b) Close-up view of the active site pocket. Those residues lying within ~3.6 Å of the bound ligands are displayed with gold bonds, whereas the ligands are depicted with blue bonds. Residues selected for site-directed mutagenesis are depicted with red labels. The magnesium ion is shown as a green sphere, and interactions with it and its ligands are represented by dashed lines. Possible hydrogen bonding interactions between the protein and the ligands are also indicated as dashed lines. Ordered water molecules are depicted as red spheres.

Table 3: Kinetic and Thermodynamic Parameters[a]

	V_{max}[b] (μmol min^{-1} mg^{-1})	K_m for AIR[b] (μM)	K_d[c] (μM)	k_{cat}[d] (min^{-1})	k_{cat}/K_m (μM^{-1} min^{-1})
wild type	50 ± 3	25 ± 5	20 ± 8	4140 ± 250	330 ± 70
D153A	0.03 ± 0.001	40 ± 7	20 ± 3	2.50 ± 0.05	0.12 ± 0.02
R155A	6 ± 0.5	180 ± 40	1.6 ± 0.5	510 ± 40	6.0 ± 1
Y152A	1.0 ± 0.2	460 ± 120	50 ± 20	110 ± 20	0.50 ± 0.2
E73A	0.03 ± 0.003	140 ± 40	9 ± 4	2.5 ± 0.3	0.04 ± 0.01
K353A	inactive[e]	NA	20 ± 5	NA	NA

[a] Reported errors are those obtained from curve fitting the appropriate data set. [b] Steady-state values were determined using the ATP-coupled assay system with the concentration of ATP and bicarbonate fixed and the concentration of AIR varied. [c] Calculated from equilibrium dialysis experiments using eq 1. [d] Calculated using the molecular weight of the dimer. Calculations were conducted assuming that 100% of the protein was active. [e] No measurable activity up to a protein concentration of 725 μg/mL.

Each residue was mutated to alanine, and the resulting proteins were analyzed by steady-state kinetics and equilibrium dialysis. The results of these studies are listed in Table 3.

Scheme 2

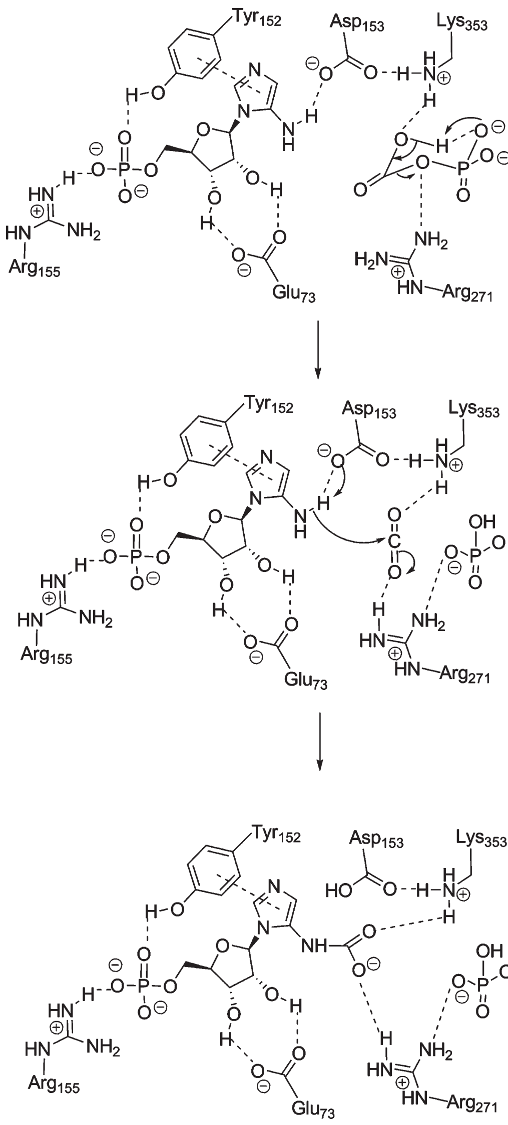

The kinetic parameters for the wild-type enzyme revealed that all of the mutations decreased the catalytic proficiency of the enzyme by 50−8000-fold. The K_m for AIR for the mutant proteins increased, yet surprisingly, for most, the K_d for AIR remained either unchanged or decreased. While there are kinetic reasons why K_m and K_d may not be equivalent, we expected that mutations in the substrate binding site would weaken the binding of AIR. The most likely explanation for the lower K_d value is that for some mutant proteins, AIR can adopt nonproductive conformations in the active site, which generated additional binding contacts at the expense of catalysis. The equilibrium dialysis experiments also indicated that for all proteins, the active enzyme concentration (based upon curve fitting using eq 1) in the dialysis experiment was 50−80% lower than the total concentration of protein added. This indicates that either not all of the protein in solution existed in the proper conformation for substrate binding or multiple substrate molecules bind to the proteins in the absence of ATP. We are currently conducting additional experiments to clarify this result.

Mutation of Tyr 152 resulted in an increase in the K_m and K_d values. This residue is of particular interest given the recent discovery that substitution of a tyrosine at the appropriate location in the *E. coli purT*-encoded glycinamide ribonucleotide transformylase confers N^5-CAIR synthetase activity to the enzyme (*23*). As noted above, Tyr 152 forms a hydrogen bond to the phosphate group of AIR and also stacks with its imidazole ring. These interactions serve to lock the substrate into a productive conformation needed for catalysis and likely enhance the specificity of N^5-CAIR synthetase for an aromatic substrate.

The Glu 73 mutant is also of interest. This residue hydrogen bonds to the 2- and 3-hydroxyl groups of the AIR ribose and is distal to the site of catalysis. Thus, we were surprised to observe a decrease in K_d and a 1400-fold decrease in k_{cat} compared to those of the wild-type enzyme. An examination of the MgADP·AIR structure reveals no direct contact with any residue believed to be involved in catalysis. Glu 73, however, is in the same loop as Glu 75 which hydrogen bonds to Arg 271. Arg 271 is located in the putative catalytic region of the active site, and as discussed below, we believe that Arg 271 plays an important role in carboxyphosphate binding and in catalysis of this intermediate. Thus, in the presence of a substrate, Glu 73 could possibly stabilize this loop and thus align Arg 271 for catalysis.

One of the goals of this study was to identify the active site base required for catalysis. Our previous work, based upon a model of the substrate-binding site in the *E. coli* enzyme, suggested that either Asp 153 or Lys 353 could function as the base. The data presented here reveal that Lys 353 is ~4 Å from the exocyclic amine of AIR, whereas Asp 153 is only 3 Å distant. Site-directed mutagenesis, steady-state kinetic analysis, and equilibrium dialysis support this conclusion. Replacement of Asp with alanine results in an enzyme with essentially the same K_m and K_d as the wild-type enzyme, but with a k_{cat} value more than 1600-fold lower. Clearly, Asp 153 is involved in catalysis, but not substrate binding. Mutation of Lys 353 to alanine also generated an inactive enzyme. The mutant protein, however, was capable of binding AIR with the same affinity as the wild-type enzyme. On the basis of our structural information, we suggest that Lys 353 is too distant to function as the catalytic base and likely plays another role in catalysis. However, we recognize that we do not have definitive kinetic evidence to rule out Lys 353 as the active site base.

Implications for the Catalytic Mechanism. N^5-CAIR synthetase is believed to catalyze the conversion of AIR into N^5-CAIR by the use of the unstable, high-energy intermediate carboxyphosphate (*13*). Once carboxyphosphate has been generated from ATP and bicarbonate, its role in the remainder of the reaction is uncertain. Either it is directly attacked by AIR, or it decomposes to generate CO_2, which then reacts with AIR to generate N^5-CAIR. Previously, we proposed a mechanism for N^5-CAIR synthetase based upon the structure of the *E. coli* enzyme complexed with MgADP and P_i (*18*). This mechanism relied upon molecular modeling to identify the location of the AIR binding site. Importantly, the structural information presented in this paper correlates exceedingly well with the originally proposed model.

The site-directed mutagenesis data presented here now allow us to add new detail to our published catalytic mechanism by assigning roles for individual amino acids in both substrate binding and catalysis as highlighted in Scheme 2. Specifically, the catalytic mechanism begins with the reaction of bicarbonate and ATP to generate carboxyphosphate and ADP. Molecular mechanics calculations suggest that the carboxyphosphate intermediate is more stable in the pseudochair conformation (*18*) as

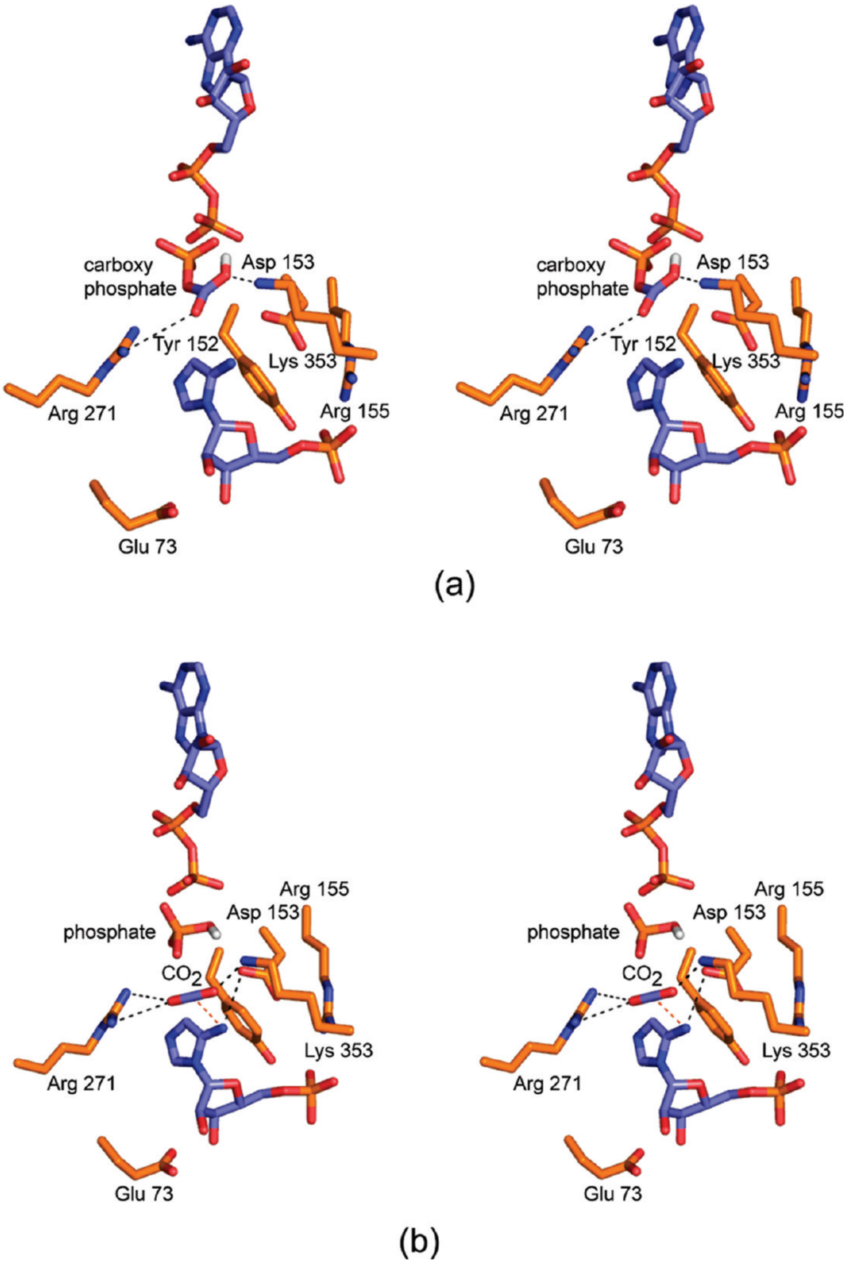

FIGURE 4: Models of proposed intermediates, carboxyphosphate and CO_2, bound in the active site of N^5-CAIR synthetase. (a) Model of carboxyphosphate bound in the active site of the enzyme. The model was generated by superimposing the structure of carboxyphosphate onto the structure of inorganic phosphate taken from the crystal structure of *E. coli* N^5-CAIR synthetase. Residues derived from the protein are shown with gold bonds, whereas AIR and ADP are highlighted with blue bonds. Hydrogen bonds between carboxyphosphate and Arg 271 and Lys 353 are represented as dashed lines. (b) Model of CO_2, created by the decomposition of carboxyphosphate, in the active site of the enzyme. Enzyme residues are shown with gold bonds, whereas AIR and ADP are displayed with blue bonds. Possible hydrogen bonds between CO_2 and Arg 271 and Lys 353 are represented as dashed lines. Possible hydrogen bonds between the exocyclic amine of AIR and Asp 153 are also shown as dashed lines. The red dashed line between the exocyclic amine of AIR and the carbon of CO_2 is meant to emphasize the direction of nucleophilic attack.

drawn in Scheme 2. By overlaying the model of the *E. coli* MgADP·P_i·N^5-CAIR synthetase complex with the *A. clavatus* MgADP·AIR structure, we generated a possible location for the carboxyphosphate intermediate, based upon the location of inorganic phosphate (*18*) (Figure 4a). On the basis of this modeling, it appears that the carboxyphosphate interacts with both Arg 271 and Lys 353. Note, however, that in this model the distance between the exocyclic amine of AIR and the carbonyl carbon of carboxyphosphate is 3.6 Å and the angle of approach is incorrect, thus suggesting that AIR does not directly attack carboxyphosphate. Instead, we suggest that carboxyphosphate decomposes to CO_2 via an intramolecular proton abstraction by the phosphate group (Scheme 2). This deprotonation and subsequent release of HPO_4^- is aided by both Arg 271 and Lys 353. Molecular modeling reveals that the CO_2 generated is directly positioned between Arg 271 and Lys 353, where each residue could form a hydrogen bond to the oxygen atoms of CO_2 (Figure 4b). These residues, which likely are positively charged, could also serve to enhance the electrophilicity of CO_2 by drawing electrons away from the carbon atom. An examination of the model presented in Figure 4b indicates that CO_2 is ~2.7 Å from the amine of AIR, and there is an optimal alignment between the amine and the carbon of CO_2. Catalysis occurs in a concerted fashion as the amine of AIR attacks the carbon of CO_2 and Asp 153 removes its proton.

The resulting negative charge on the oxygen atom is stabilized by either Arg 271 or Lys 353 (Scheme 2).

In summary, the results presented here provide, for the first time, detailed molecular information regarding the binding of AIR to N^5-CAIR synthetase. Furthermore, this study is the first to present structural information on any N^5-CAIR synthetase isolated from lower eukaryotes. Such knowledge has given us the ability to rationally select amino acids for mutation, and we have demonstrated that both Asp 153 and Lys 353 are critical for catalysis. These data provide a more detailed understanding of the enzyme, which in turn, will help in the design of novel antibacterial and antifungal agents.

ACKNOWLEDGMENT

We thank Drs. W. W. Cleland and Grover Waldrop for insightful comments.

REFERENCES

1. Wright, G. D. (2007) The antibiotic resistome: The nexus of chemical and genetic diversity. *Nat. Rev. Microbiol. 5*, 175–186.
2. Walsh, C. (2003) Where will new antibiotics come from? *Nat. Rev. Microbiol. 1*, 65–70.
3. Alekshun, M. N. (2005) New advances in antibiotic development and discovery. *Expert Opin. Invest. Drugs 14*, 117–134.
4. Spellberg, B., Powers, J. H., Brass, E. P., Miller, L. G., and Edwards, J. E., Jr. (2004) Trends in antimicrobial drug development: Implications for the future. *Clin. Infect. Dis. 38*, 1279–1286.
5. Appelbaum, P. C. (2006) MRSA: The tip of the iceberg. *Clin. Microbiol. Infect. 12* (Suppl. 2), 3–10.
6. National Nosocomial Infections Surveillance System (2004) National Nosocomial Infections Surveillance (NNIS) System Report, data summary from January 1992 through June 2004, issued October 2004. *Am. J. Infect. Control 32*, 470–485.
7. Choudhry, A. E., Mandichak, T. L., Broskey, J. P., Egolf, R. W., Kinsland, C., Begley, T. P., Seefeld, M. A., Ku, T. W., Brown, J. R., Zalacain, M., and Ratnam, K. (2003) Inhibitors of pantothenate kinase: Novel antibiotics for *staphylococcal* infections. *Antimicrob. Agents Chemother. 47*, 2051–2055.
8. Beyer, D., Kroll, H. P., Endermann, R., Schiffer, G., Siegel, S., Bauser, M., Pohlmann, J., Brands, M., Ziegelbauer, K., Haebich, D., Eymann, C., and Brotz-Oesterhelt, H. (2004) New class of bacterial phenylalanyl-tRNA synthetase inhibitors with high potency and broad-spectrum activity. *Antimicrob. Agents Chemother. 48*, 525–532.
9. Brotz-Oesterhelt, H., Knezevic, I., Bartel, S., Lampe, T., Warnecke-Eberz, U., Ziegelbauer, K., Habich, D., and Labischinski, H. (2003) Specific and potent inhibition of NAD^+-dependent DNA ligase by pyridochromanones. *J. Biol. Chem. 278*, 39435–39442.
10. Kuntz, L., Tritsch, D., Grosdemange-Billiard, C., Hemmerlin, A., Willem, A., Bach, T. J., and Rohmer, M. (2005) Isoprenoid biosynthesis as a target for antibacterial and antiparasitic drugs: Phosphonohydroxamic acids as inhibitors of deoxyxylulose phosphate reductoisomerase. *Biochem. J. 386*, 127–135.
11. Bulloch, E. M., Jones, M. A., Parker, E. J., Osborne, A. P., Stephens, E., Davies, G. M., Coggins, J. R., and Abell, C. (2004) Identification of 4-amino-4-deoxychorismate synthase as the molecular target for the antimicrobial action of (6*S*)-6-fluoroshikimate. *J. Am. Chem. Soc. 126*, 9912–9913.
12. Meyer, E., Leonard, N. J., Bhat, B., Stubbe, J., and Smith, J. M. (1992) Purification and characterization of the purE, purK, and purC gene products: Identification of a previously unrecognized energy requirement in the purine biosynthetic pathway. *Biochemistry 31*, 5022–5032.
13. Mueller, E. J., Meyer, E., Rudolph, J., Davisson, V. J., and Stubbe, J. (1994) N5-Carboxyaminoimidazole ribonucleotide: Evidence for a new intermediate and two new enzymatic activities in the de novo purine biosynthetic pathway of *Escherichia coli*. *Biochemistry 33*, 2269–2278.
14. Firestine, S. M., and Davisson, V. J. (1994) Carboxylases in *de novo* purine biosynthesis. Characterization of the *Gallus gallus* bifunctional enzyme. *Biochemistry 33*, 11917–11926.
15. Firestine, S. (1995) Biochemical and mechanistic characterization of *Gallus gallus* 5-aminoimidazole ribonucleotide carboxylase, Ph.D. Thesis, Purdue University, West Lafayette, IN.
16. Firestine, S. M., Misialek, S., Toffaletti, D. L., Klem, T. J., Perfect, J. R., and Davisson, V. J. (1998) Biochemical role of the *Cryptococcus neoformans* ADE2 protein in fungal *de novo* purine biosynthesis. *Arch. Biochem. Biophys. 351*, 123–134.
17. Firestine, S. M., Paritala, H., McDonnell, J. E., Thoden, J. B., and Holden, H. M. (2009) Identification of inhibitors of N^5-carboxyaminoimidazole ribonucleotide synthetase by high-throughput screening. *Bioorg. Med. Chem. 17*, 3317–3323.
18. Thoden, J. B., Holden, H. M., and Firestine, S. M. (2008) Structural analysis of the active site geometry of N^5-carboxyaminoimidazole ribonucleotide synthetase from *Escherichia coli*. *Biochemistry 47*, 13346–13353.
19. McCoy, A. J., Grosse-Kunstleve, R. W., Adams, P. D., Winn, M. D., Storoni, L. C., and Read, R. J. (2007) Phaser crystallographic software. *J. Appl. Crystallogr. 40*, 658–674.
20. Cowtan, K. (1994) 'dm:' An automated procedure for phase improvement by density modification. *Joint CCP4 and ESF-EACBM Newsletter on Protein Crystallography 31*, 34–38.
21. Emsley, P., and Cowtan, K. (2004) Coot: Model-building tools for molecular graphics. *Acta Crystallogr. D60*, 2126–2132.
22. Tronrud, D. E., Ten Eyck, L. F., and Matthews, B. W. (1987) An efficient general-purpose least-squares refinement program for macromolecular structures. *Acta Crystallogr. A43*, 489–501.
23. Li, H., Fast, W., and Benkovic, S. J. (2009) Structural and functional modularity of proteins in the *de novo* purine biosynthetic pathway. *Protein Sci. 18*, 881–892.
24. DeLano, W. L. (2002) The PyMOL Molecular Graphics System, DeLano Scientific, San Carlos, CA.